Theoretical concepts of unlimited-power reflectors, absorbers, and emitters with conjugately matched layers

Constantinos A. Valagiannopoulos[1] and Sergei A. Tretyakov[2]

[1]*Department of Physics, School of Science and Technology, Nazarbayev University, KZ-010000, Astana, Kazakhstan*

[2]*Department of Radio Science and Engineering, School of Electrical Engineering, Aalto University, P. O. Box 13000, FI-00076 Aalto, Finland*

(Received 20 April 2016; revised manuscript received 8 August 2016; published xxxxxx)

Recently, it was shown that by using special artificial materials it is possible to ensure that all electromagnetic modes of free space are conjugately matched to the modes of a material body and, thus, all modes deliver power to the body in the most effective way. Such a fascinating feature is acquired because the conjugate matching does not concern only the propagating modes but, most importantly, is applied to all evanescent modes; in this way, all the possible ways of transferring the electromagnetic energy to the material body can be optimally exploited. However, coupling to higher-order (mostly evanescent) modes is weak and totally disappears in the limit of an infinite planar boundary. Here, we show that by properly perturbing the surface of the receiving or emitting body with, for example, randomly distributed small particles, we can open up channels for super-radiation into the far zone. The currents induced in the small particles act as secondary sources (radiation "vessels") which send the energy to travel far away from the surface and, reciprocally, receive power from far-located sources. For a particular example, we theoretically predict about 20-fold power transfer enhancement between the conjugately matched power-receiving body (as compared with the ideal black body) and far-zone sources. Reciprocally, the proposed structure radiates about 20 times more power into the far zone as compared with the same source over a perfect reflector.

DOI: 10.1103/PhysRevB.00.005100

I. INTRODUCTION

The problem of optimizing and maximizing absorption and emission of electromagnetic energy is relevant for a broad variety of applications such as antennas, radar absorbers, thermal emitters and accumulators, photovoltaic devices, and more [1–8]. For macroscopic bodies (having sizes large compared to the wavelength of electromagnetic radiation), it is usually assumed that the ultimate absorber and emitter is the ideal black body that completely absorbs all incident rays (e.g., [9]). Conceptually, ideal black body, introduced by Kirchhoff [10], is totally opaque and has zero reflection coefficient for any propagating plane wave (any incidence angle and any polarization); in this sense, it is the perfect absorber of electromagnetic energy. Following the Planck theory of thermal radiation [11], the ideal black body appears to be also the ultimate thermal emitter for radiating heat into free space. Practical realization of bodies whose properties mimic those of ideal black bodies is a scientific and technical challenge (see, e.g., [2,3]).

However, it has been recently demonstrated that, in principle, it is possible to engineer bodies which can absorb power not only from incident propagating waves (incident rays in the Kirchhoff black-body concept), but also from external evanescent fields or high-order spherical harmonics of the incident-wave spectrum [12,13]. Due to the resonant nature of surface modes of these superabsorbing and superemitting bodies, their absorption cross section grows without limit when the medium parameters approach the ideal values, and the thermal spectral emissivity at the resonance frequency becomes arbitrarily high compared to Planck's black body of the same size and the same temperature. The material structures proposed in [12,13] realize the ideas of conjugate matching of all modes of free space to all modes of the absorbing/emitting body [8,14,15], and we call them *conjugately matched* bodies or layers (CML).

The material realizations proposed in [12,13] are based on the use of double-negative (DNG) isotropic or uniaxial media which obey the uniaxial perfectly matched layer (PML) conditions [16]. High-order modes of conjugately matched bodies [12,13] resonate with all modes of free space and most effectively exchange energy with them. However, to effectively absorb or emit all the modes, it is necessary that the modes of the body are sufficiently coupled with the corresponding modes of free space. In [12], it is shown that if a conjugately matched body fills a half-space (a planar infinite interface with free space), its properties are the same as of the conventional ideal black body and no absorption or radiation enhancement over the ideal black-body limit can take place. To couple with higher-order free-space modes, we can make the surface not planar, and in [12] it is shown that for bodies of finite sizes, on an example of a sphere, unlimited power exchange power is indeed possible. An alternative scenario was explored in paper [13], where the conjugately matched body filled a half-space with an infinite planar interface, but the sources in free space were positioned close to the interface and created large evanescent fields which directly couple to the resonant surface modes of the conjugately matched layer. Also in this case it was seen that the absorption in the body was dramatically stronger than in an ideal black body at the same position.

In this paper, we show that it is possible to realize an infinite and planar surface which can absorb and emit more power than the ideal black body by perturbing the surface of a conjugately matched layer, introduced in [13]. In this scenario, small subwavelength scatterers randomly distributed over the body surface offer necessary coupling between high-order resonant surface modes and the far-zone fields, opening channels for extra absorption or emission of energy. In the limit of ideal material parameters, this planar interface not only absorbs or reflects all incident propagating waves, but does the same also for all evanescent harmonics. We show that a perturbed

 ©2016 American Physical Society

interface with a low-loss conjugately matched body acts as a "super-reflector" of fields developed from a small antenna in its vicinity by launching the energy stored in the antenna near field into space.

In particular, we introduce a random grid of electrically thin cylinders close to a resonant interface with a conjugately matched layer, where huge reactive energy is stored. Inevitably, currents induced in thin conductive cylinders radiate into far zone as linear antennas, and we say that these cylinders act as radiation "vessels." A random and sparse enough distribution of cylinders ensures that diffuse radiation survives in the far zone and is not coherently combined into a plane wave. We test the effects of this cluster of particles on the radiation from various conjugately matched layers and conclude that for a realizable passive structure, one can achieve a stable 20–30-fold enhancement of the far-field power.

Such super-reflectors are extremely strongly coupled to evanescent fields of external sources and can extract power from them in the most efficient way. In the antenna terminology, the effective area of the CML reflector is larger than the geometrical one, although the reflector size is very large compared with the wavelength. Basically, we aim at realization of a surface which (at its resonant frequency) would be "more reflective than the ideal perfectly conducting mirror," and this property would hold even in the limit of the infinite planar reflector. If the perturbing elements are lossy, instead of enhancing reflection we can enhance absorption in a planar absorbing layer or enhance thermal radiation from a planar hot surface into the far zone beyond the Planck limit of the ideal black body. We expect that perturbing the surface can be a more effective mean to couple to far-zone field as compared to curved surfaces. In the study [12] it was expectedly found that for large spherical bodies, when the curvature of the surface becomes small, one needs extreme (low-loss) values of material parameters in order to realize enough effective coupling to high-order harmonics. The surface perturbation approach, introduced here, does not have this limitation.

II. CONJUGATELY MATCHED LAYER (CML)

We begin the study by a brief explanation of the concept of the conjugately matched layer, introduced in [13]. It has been recently reported [12,13] that there can exist material bodies which optimally absorb energy of electromagnetic fields, by achieving conjugate matching for every free-space mode. In the theoretical limit of negligible losses in the absorbing body, such an optimally designed finite-sized body can absorb the whole infinite energy of an incident propagating plane wave [12]. In [13], a uniaxial medium with special values for its constituent parameters has been suggested as possible realization. The permittivities and permeabilities (transversal with subscript t and normal to the material sample boundary with subscript n) satisfy the uniaxial perfectly matched layer (PML) conditions [16–20] and simultaneously possess negative real parts as in a double-negative (DNG) medium [21], contrary to the conventional uniaxial PML choice. For planar interfaces and TM polarization (sole magnetic component parallel to the half-space boundary), the material parameters satisfy

$$\varepsilon_t = \mu_t = \frac{1}{\varepsilon_n} = a - jb, \tag{1}$$

where a and b are real parameters and $a < 0$. We assume harmonic time dependence $\exp(+j\omega t)$, where ω is the angular operating frequency and j is the imaginary unit. The parameter $b > 0$ corresponds to losses for propagating plane waves, and it is easy to show [16,26] that sufficiently thick slabs of such materials behave as perfect absorbers for arbitrary incident propagating plane waves. From duality, a similar expression for the parameters of uniaxial perfect absorbers holds for the fields of the TE polarization: $\varepsilon_t = \mu_t = \frac{1}{\mu_n} = a - jb$. To ensure that the thought properties hold for both orthogonal polarizations, we can require that $\varepsilon_n = \mu_n$. For compactness, in the following we present only formulas for the TM polarization, without compromising the generality.

Any uniaxial medium characterized by the constituent parameters $(\varepsilon_t, \mu_t, \varepsilon_n)$ has the following TM wave impedance Z (e.g., [26]):

$$Z = -j\frac{\eta_0}{k_0\varepsilon_t}\sqrt{\frac{\varepsilon_t}{\varepsilon_n}k_t^2 - \varepsilon_t\mu_t k_0^2}, \tag{2}$$

which relates the tangential to the interface components of electric and magnetic fields of plane waves in the medium. The notations $\eta_0 = \sqrt{\mu_0/\varepsilon_0}$ and $k_0 = \omega\sqrt{\varepsilon_0\mu_0} = 2\pi/\lambda_0$ correspond to the free-space wave impedance and wave number, respectively (ε_0 and μ_0 are the permittivity and permeability of vacuum, while λ_0 is the operational wavelength in free space). The symbol k_t is used for the transversal wave number of the incident plane wave. Vector $\mathbf{k}_t$ is parallel to the boundary of the half-space and normal to the sole component of magnetic field. The basic property of a material with the constituent parameters given by (1) when $a < 0$ is that its wave impedance Z is the complex conjugate of the TM wave impedance of vacuum $Z^* = Z_0 = -j\frac{\eta_0}{k_0}\sqrt{k_t^2 - k_0^2}$ [13].

Most importantly, this equality is valid for every real wave number $k_t \in \mathbb{R}$, either of a propagating wave in free space ($|k_t| < k_0$) or of an evanescent mode ($|k_t| > k_0$). Therefore, the use of such conjugately matched layers (CLM), as we call them, leads to maximal power transfer from arbitrary incident fields into the medium since they optimally use every possible way (mode) available from sources outside of the material sample. Actually, in this ideal case of overall lossless conjugately matched medium, fields tend to infinity at the material surface. Assuming infinitesimally small losses in the CML, infinite power can be delivered to the medium, provided that the incident evanescent field is created by an antenna fed by an ideal voltage or current source, capable of supplying infinite power. In other words, the CML structure is identical to ordinary PML for $|k_t| < k_0$ but operates totally differently for $|k_t| > k_0$ aiming not at zero reflection but at the maximal power transfer.

By inspection of (1), one can directly infer that if $b > 0$, the transversal relative constituent parameters ε_t, μ_t, are lossy; however, the normal component of the permittivity ε_n is an active one. In order to identify the overall character of the uniaxial medium, we consider a perturbed version of the ideal material parameter values by using a small additional

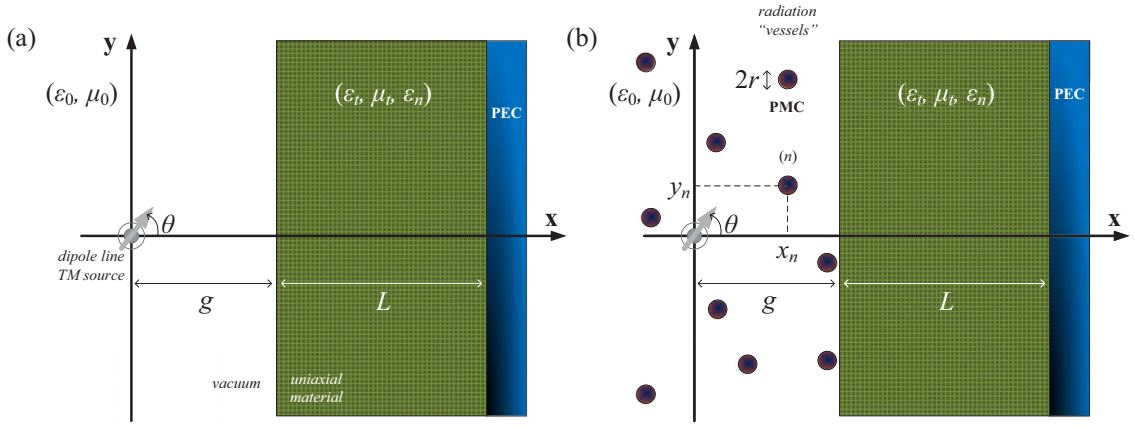

FIG. 1. (a) The testbed configuration of a grounded electrically thick slab filled with a uniaxial material $(\varepsilon_t, \mu_t, \varepsilon_n)$ with the thickness L, excited by a TM electric dipole line inclined by the angle θ located at a small distance g from the air-medium interface. (b) The same structure in the presence of a cluster of N electrically thin (the radius r) circular perfect magnetic conductor (PMC) cylinders randomly distributed in the vicinity of the air-slab interface with arbitrary coordinates (x_n, y_n) for $n = 1, \ldots, N$.

parameter δ controlling the imaginary part of the normal permittivity $\varepsilon_n = \frac{1}{\varepsilon_t} - j\delta = \frac{1}{a-jb} - j\delta$, which tends to the ideal CML medium parameters for $\delta \to 0$. To study the properties of such a quasi-CML medium, we use the testbed configuration illustrated in Fig. 1(a). For simplicity of analytical considerations, we assume that there is no dependence on one of the tangential coordinates (z). A grounded slab of the thickness L, filled with a uniaxial material with the constituent parameters $(\varepsilon_t, \mu_t, \varepsilon_n)$, is excited by an infinite electric-dipole line located at the distance g from the air-medium interface. The exciting dipole moments are orthogonal to the axis z and inclined by the angle θ with respect to the axis x [Fig. 1(a)]. In this configuration, the magnetic field has only one nonzero component (along z) and the fields are TM polarized.

In [13], an approximate analytical formula for the absorbed power (per unit length along the $\hat{\mathbf{z}}$ axis) has been derived. It shows that the absorbed power P is a sum of two terms. The first term corresponds to the power delivered by the propagating modes $P_{\text{prop}} = \mu_0 \omega^3 q^2/16$, and it is independent from the angle θ. Here, q is the electric dipole moment per unit length of the line (measured in Coulomb). The second term gives the power absorbed from the evanescent-modes fields and is written as [13]

$$P_{\text{evan}} \cong P_{\text{prop}} \frac{8|a|}{k_0^2 \pi} \int_{k_0}^{+\infty} \frac{k_t^2 \left(k_t^2 - k_0^2 \sin^2\theta\right)}{\left(k_t^2 - k_0^2\right)^{3/2}} e^{-2g\sqrt{k_t^2 - k_0^2}} \times \frac{\delta}{[1 + \text{sgn}(a)]^2 + \delta^2 \left[\frac{k_t^2 |\varepsilon_t|}{2(k_t^2 - k_0^2)}\right]^2} dk_t \qquad (3)$$

for $\delta \to 0$. It is noteworthy that the CML slab acts as an ultraefficient passive absorber ($P \to +\infty$) of the incoming illumination for $\delta > 0$ and as an infinite-power active emitter ($P \to -\infty$) for $\delta < 0$. In the limit of $\delta \to 0^+$, both the field strength at the surface and the absorbed power diverge and tend to infinity. Therefore, it would be meaningful to inspect the field distributions leading to such unbounded field concentrations.

III. EXCITATION OF CML

Let us examine the fields created by a small source in the vicinity of an infinite and homogeneous CML slab within the testbed setup shown in Fig. 1(a). The corresponding boundary-value problem is scalar, and the magnetic field possesses a sole component parallel to $\hat{\mathbf{z}}$ axis [$\mathbf{H} = \hat{\mathbf{z}} H(x,y)$]. The used Cartesian coordinate system (x,y,z) is also defined in Fig. 1(a), with the primary dipole line source positioned at $(x,y) = (0,0)$. The incident magnetic field from that electric-dipole line (existing in vacuum) can be expressed in the following integral form [22]:

$$H_{\text{inc}}(x,y) = -\frac{\omega q}{4\pi} \int_{-\infty}^{+\infty} e^{-|x|\kappa_0(k_t)} \times \left[\frac{k_t}{\kappa_0(k_t)} \cos\theta + j \sin\theta \, \text{sgn}(x)\right] e^{-jk_t y} dk_t, \qquad (4)$$

where the normal to the interface component of the wave number $\kappa_0(k_t) = \sqrt{k_t^2 - k_0^2}$ is evaluated with a positive real part and if the real part is zero, as a positive imaginary number. Analytical expression for the incident field involving Hankel function [22,23] is also available but not given here for brevity since all the field quantities are expressed as spectral integrals.

The formulated boundary-value problem can be solved analytically. As a result, we find that the secondary field developed due to the presence of the uniaxial slab and the PEC plane in free space ($x < g$) is given by $H_{\text{sec}}(x,y) = \int_{-\infty}^{+\infty} S_{\text{sec}}(k_t) e^{\kappa_0(k_t)x - jk_t y} dk_t$, where

$$S_{\text{sec}}(k_t) = \frac{\omega q}{4\pi} e^{-2g\kappa_0(k_t)} \left(\frac{k_t}{\kappa_0(k_t)} \cos\theta + j \sin\theta\right) \times \frac{\kappa(k_t) - \varepsilon_t \coth[\kappa(k_t)L]\kappa_0(k_t)}{\kappa(k_t) + \varepsilon_t \coth[\kappa(k_t)L]\kappa_0(k_t)}. \qquad (5)$$

The value of

$$\kappa(k_t) = \sqrt{k_t^2 \frac{\varepsilon_t}{\varepsilon_n} - k_0^2 \varepsilon_t \mu_t} \qquad (6)$$

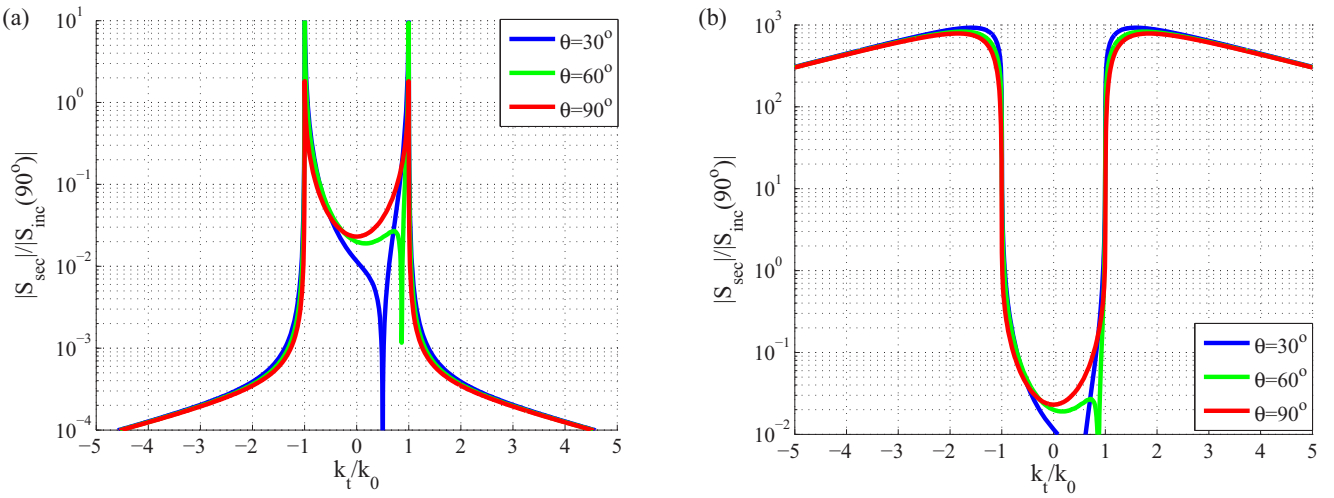

FIG. 2. The magnitude of the spatial spectral density function of the secondary field $S_{\text{sec}}(k_t)$ at $x = 0$ with respect to the normalized wave number k_t/k_0 for various inclination angles θ and (a) $a = 2$ (DPS-PML) and (b) $a = -2$ (CML). Common plot parameters: $b = 0.1, \delta = 0.001$, $g = 0.03\lambda_0$, $L = 3\lambda_0$. The represented quantity is normalized by $S_{\text{inc}}(90^\circ) = j\omega q/(4\pi)$.

is the normal component of the plane-wave propagation constant in the CML slab. The total field in vacuum equals to $H_{\text{back}}(x,y) = H_{\text{inc}}(x,y) + H_{\text{sec}}(x,y)$.

In Fig. 2, we present the magnitude of the integrand in the formula of the secondary magnetic field for $x = 0$ (very close to the air-CML boundary located at $x = g$), equal to $|S_{\text{sec}}(k_t)|$ as a function of the normalized transversal wave number k_t/k_0 for various inclination angles of the source θ. The presented quantity is normalized by the (constant) magnitude of the integrand of the incident field (4) for $\theta = 90^\circ$: $S_{\text{inc}}(90^\circ) = \frac{j\omega q}{4\pi}$, which is independent from k_t and gives us a metric of the incident power. Figure 2(a) corresponds to a double-positive (DPS) conventional uniaxial PML [16] and it is directly observed that $|S_{\text{sec}}|$ vanishes exponentially for evanescent waves ($|k_t| > k_0$). On the contrary, for the CML case [Fig. 2(b)], the integrand values have huge magnitudes for $|k_t| > k_0$ regardless of the angle θ. These graphs verify the aforementioned theoretical expectation that unbounded absorbed power of (3) in the CML case ($a < 0$ and $|\delta| \to 0$) is due to the extremely large magnitudes of the evanescent fields developed in the vicinity of the interface, as demonstrated by Fig. 2(b). Note the different scale in Figs. 2(a) and 2(b): the values in the region $-1 < k_t/k_0 < 1$, which correspond to the propagating-wave part of the spectrum, are the same in both figures.

Figure 3 shows the spatial distribution of the total magnetic field $|H_{\text{back}}(x,y)|$ for the two cases of Fig. 2 (with $\theta = 90^\circ$). The represented quantity is normalized by the value of the incident field at $(x,y) = (g,0)$ and is expressed in dB. We again observe how more efficient is the CML medium

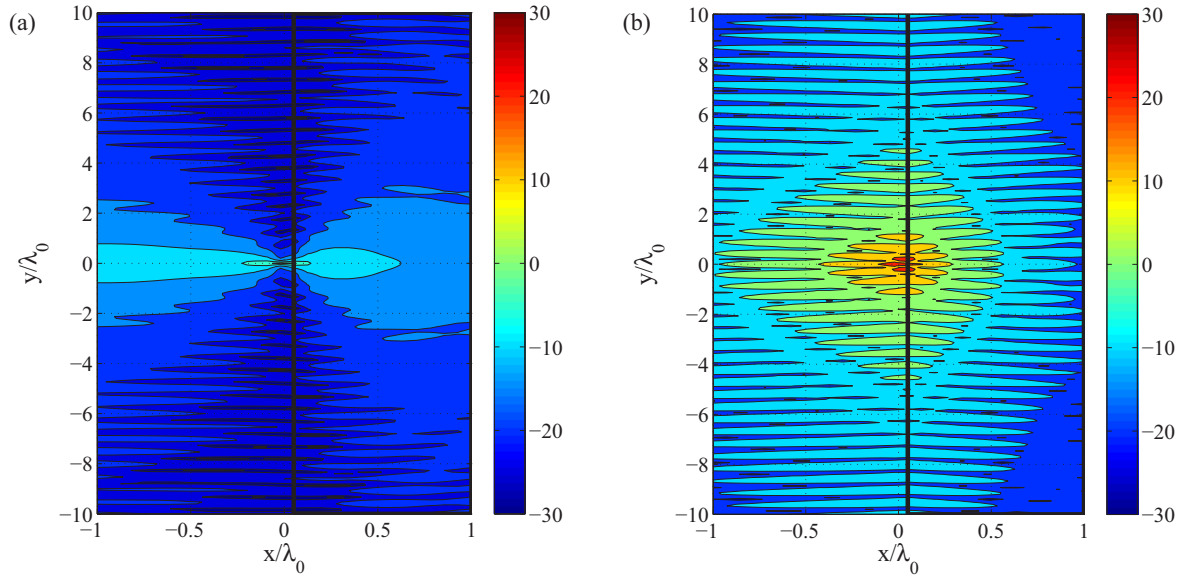

FIG. 3. The spatial distributions of the total magnetic field $H_{\text{back}}(x,y)$ normalized by $H_{\text{inc}}(g,0)$ expressed in dB for (a) $a = 2$ (DPS-PML) and (b) $a = -2$ (CML). Common plot parameters: $b = 0.1, \delta = 0.001, g = 0.03\lambda_0, L = 3\lambda_0, \theta = 90^\circ$.

[Fig. 2(b)] in exciting fields along its boundary compared to the conventional PML case [Fig. 2(a)]. However, since the nature of these fields is evanescent, they are rapidly decaying with increasing the distance from the surface ($x \to -\infty$). It should be stressed that the concentration of the fields in the vicinity of the CML interface is always huge regardless of the sign of δ, both for overall passive ($\delta > 0$) or active ($\delta < 0$) structures.

In this paper, we propose to make use of this concentration of fields along the boundary of the two regions ($x = g$) to create an "antenna," which would "launch" the energy stored in this region into the far zone $x \to -\infty$. This is not an easy task, though. It is well known that resonant surface modes along infinite and regular surfaces do not radiate energy into the far zone. In other words, despite the huge difference of the two systems (PML versus CML slab) in the near field, the behavior of the field radiated in the far region is similar. Actually, with the use of the stationary phase method, one can directly evaluate the azimuthal profiles of the incident and the secondary fields in the far zone as follows:

$$h_{\text{inc}}(\varphi) \sim \frac{k_0 j\omega q}{4} \sin(\varphi - \theta), \qquad x \to -\infty, \tag{7}$$

$$h_{\text{sec}}(\varphi) \sim -\pi k_0 S_{\text{sec}}(k_0 \sin\varphi) \cos\varphi, \qquad x \to -\infty, \tag{8}$$

for $90^\circ < \varphi < 270^\circ$. We notice that the expression of the secondary component, which describes the effect of the grounded slab, is proportional to a specific value of the function $S_{\text{sec}}(k_t)$: the one corresponding to $k_t = k_0 \sin\varphi$. Since this value is always smaller in magnitude than k_0 ($\varphi \in \mathbb{R}$), namely, corresponding to a propagating and not to an evanescent mode, it is clear that huge reactive fields of Fig. 2(b) do not to contribute to far-zone radiation. The situation is not the same if one uses as an electromagnetic energy sink a finite-size body filled with a suitable CML medium. In cylindrical [13] or spherical [12] cases, there are no purely evanescent modes and thus all the fields contribute (poorly) to the radiative power. In the infinite slab case analyzed here, the necessity of something that can act as a radiation "vessel" to allow the field energy stored in resonant surface modes to propagate far away from the source, becomes clear.

IV. RADIATION WITH "VESSELS"

A. Circuit theory approach

In an attempt to find a way to exploit this huge field concentration and transform the sizable magnitude of evanescent modes (developed close to $x = g$) into radiative fields, we consider the configuration of Fig. 1(b). Let us randomly distribute small cylindrical scatterers in the vicinity of the air-CML slab interface. It is expected that the large evanescent fields would excite currents along these wires, which will act as radiation vessels, and their own field would be expressed as cylindrical modes which are always partially propagating and survive in the far region.

The idea of perturbing the surface with tiny scatterers can be understood from the equivalent circuit corresponding to the fields of a particular evanescent plane-wave component exciting the CML slab in presence of a small scatterer, shown in Fig. 4. The ideal voltage source V represents the primary

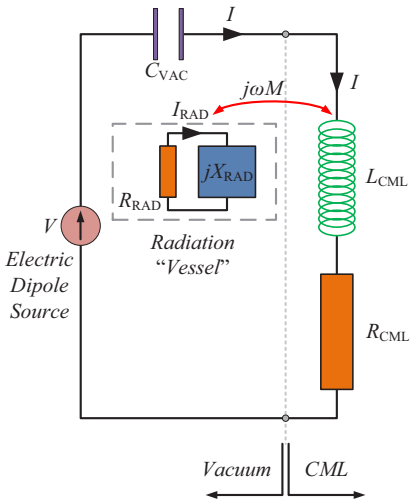

FIG. 4. Sketch of the equivalent circuit for excitation by a particular evanescent TM plane-wave component. The wave impedance of TM waves in vacuum Z_0 corresponds to the capacitance C_{VAC}, while the impedance Z of the CML contains a loss resistor R_{CML} and an inductive L_{CML} component. The cylindrical vessel in the near field of vacuum-CML interface is characterized by a radiation resistance R_{RAD} and a reactive impedance X_{RAD}.

radiator (an electric dipole source in this configuration) and capacitance C_{VAC} expresses the wave impedance of free space for a specific value of k_t, given by (2) for $\varepsilon_t = \mu_t = \varepsilon_n = 1$. The inductive complex impedance ($R_{\text{CML}} + j\omega L_{\text{CML}}$) is given by (2) with the parameters of the CML layer. Resistance R_{CML} models the dissipative losses in the CML slab and the current flown through the primary circuit is denoted by I. The small scatterer (radiation "vessel") in the vicinity of the interface is modeled by the radiation vessel circuit, of current I_{RAD}, formed by a nonresonant reactive element (jX_{RAD}) (capacitive or inductive) and a small resistor of the radiator R_{RAD}. If the scatterer is lossless, R_{RAD} corresponds to the radiation resistance, and if it is absorptive, the resistance is the sum of the radiative and dissipative terms. Near-field coupling between the scatterer and the resonant surface mode of the interface is modeled for simplicity by mutual inductance $j\omega M$. In general, the mutual impedance $j\omega M$ can be a complex number with any sign of the imaginary part; however, here we confine our analysis to a very closely positioned particle, in which case the mutual impedance is predominantly reactive ($M \in \mathbb{R}$) and inductive ($M > 0$) for the considered TM polarization.

The circuit in the absence of the radiation vessels ($M = 0$) has been analyzed in [13], and it is clear that the power delivered to the loss resistor R_{CML} tends to infinity when the series LC circuit works at resonance and under the additional condition $R_{\text{CML}} \to 0$. In other words, the absorbed power is limited only by the energy available from the primary source, while there is no radiation towards the far zone ($P_{\text{RAD}} = 0$). In the presence of the vessels, however, the systems behave dramatically different. Considering the circuit of Fig. 4, we can easily find the current amplitude both in the directly fed branch (I) and in the circuit of the radiating

vessel ($I_{\rm RAD}$):

$$I = \frac{V(R_{\rm RAD} + jX_{\rm RAD})}{\omega^2 M^2 + (R_{\rm RAD} + jX_{\rm RAD})\left(R_{\rm CML} + j\omega L_{\rm CML} + \frac{1}{j\omega C_{\rm VAC}}\right)}, \tag{9}$$

$$I_{\rm RAD} = -\frac{j\omega M V}{\omega^2 M^2 + (R_{\rm RAD} + jX_{\rm RAD})\left(R_{\rm CML} + j\omega L_{\rm CML} + \frac{1}{j\omega C_{\rm VAC}}\right)}. \tag{10}$$

If we assume that there are no particles playing the role of radiation vessels ($M = 0$), we notice that at the resonant frequency of the mode $j\omega L_{\rm CML} + \frac{1}{j\omega C_{\rm VAC}} = 0$ and in the limit of negligible losses into the CML slab $R_{\rm CML} \to 0$, the current I increases without bound. However, the radiated power $P_{\rm RAD}$ is zero because the resistance $R_{\rm CML}$ represents the dissipative process, not the radiative operation. In this way, we come again to the aforementioned conclusion that the power is accumulated in the near field and does not reach the far zone. On the contrary, when the pin comes close to the vacuum-CML interface, the radiated power equals to that delivered to $R_{\rm RAD}$ since it models the function of the vessel as antenna. Therefore,

$$P_{\rm RAD} = \frac{|V|^2}{2} \frac{\omega^2 M^2 R_{\rm RAD}}{(\omega^2 M^2 + R_{\rm RAD} R_{\rm CML})^2 + (X_{\rm RAD} R_{\rm CML})^2}, \tag{11}$$

under the assumption that the system works at CML resonant frequency, namely, $\omega = 1/\sqrt{L_{\rm CML} C_{\rm VAC}}$. For resonant and low-loss CML ($R_{\rm CML} \to 0$), the expression for the radiated power simplifies to $P_{\rm RAD} = \frac{R_{\rm RAD}|V|^2}{2\omega^2 M^2}$. It is clear that in order to enhance radiation, we need to bring the CML to resonance and reduce its losses, while the vessels can be small and nonresonant. Coupling between the scatterers and the surface modes should be weak in the scenario.

In the reciprocal situation of excitation by far-zone sources, we see that it is possible to enhance absorption beyond the ideal black-body full absorption of propagating plane waves by making the small scatterers lossy. In this case, assuming that the scatterers do not create a significant shadow for the propagating modes, the propagating plane waves deliver nearly all their power to the CML body, while the evanescent waves (high-order cylindrical harmonics) couple to the resonant surface modes via the small scatterers and deliver additional power into the loss resistors of the scatterers.

B. Electromagnetic theory approach

Having understood the basic operational principle from an equivalent circuit, which is by default an approximation for every single mode k_t, we will next solve the problem rigorously for the entire spectrum of k_t. A spectrum integral formulation is feasible if we assume random but specific positions of a finite number of scatterers (x_n, y_n) on the xy plane, where $n = 1, \ldots, N$ [as shown in Fig. 1(b)]. For the sake of simplicity of test calculations, we assume that particles are circular cylinders of a small radius r and of perfectly magnetically conducting (PMC) material. In Fig. 1(b), the pins are located even at $x < 0$ since we have implied that the distance g of the primary dipole from the interface is electrically small and thus the evanescent fields may be strong even at the left side of the source. Such a choice does not affect the presented concept since similar results can be obtained if we restrict the radiation vessels positions to the strip $0 < x < g$. We chose perfect magnetic conductor pins as a simple model of lossless scatterers supporting magnetic currents which is most appropriate for the considered TM polarization. Conceptual results will not change for any other small lossless scatterers at the same positions. Green's function of the considered configuration for both source (χ, ψ) and observation points (x, y) in vacuum is comprised of two components. The singular component is just a cylindrical wave [23]:

$$G_{\rm singular}(x, y, \chi, \psi) = -\frac{j}{4} H_0^{(2)}(k_0 \sqrt{(x-\chi)^2 + (y-\psi)^2}), \tag{12}$$

where $H_0^{(2)}$ is the Hankel function of zero order and second type. The smooth component of Green's function describes the effect of the grounded CML slab on the free-space field and is found as follows:

$$G_{\rm smooth}(x, y, \chi, \psi) = \int_{-\infty}^{+\infty} S_{\rm gre}(k_t) e^{\kappa_0(k_t)(x+\chi)} e^{-jk_t(y-\psi)} dk_t, \tag{13}$$

where the spatial spectral density is given by [24]

$$S_{\rm gre}(k_t) = \frac{1}{4\pi} \frac{e^{-2\kappa_0(k_t)g}}{\kappa_0(k_t)} \frac{\varepsilon_t \coth[\kappa(k_t)L]\kappa_0(k_t) - \kappa(k_t)}{\varepsilon_t \coth[\kappa(k_t)L]\kappa_0(k_t) + \kappa(k_t)}. \tag{14}$$

If we use the symbol M_n $(n = 1, \ldots, N)$ for the magnetic currents (measured in volt/meter) induced along the axes of the cylinders, the scattered magnetic field produced due to the presence of them is given as the following integral [25]:

$$H_{\rm scat}(x, y) = -\frac{jk_0}{\eta_0} \sum_{n=1}^{N} \int_{(C_n)} M_n(l)[G_{\rm singular}(x, y, \chi(l), \psi(l)) + G_{\rm smooth}(x, y, \chi(l), \psi(l))] dl. \tag{15}$$

The notation C_n is used for the contours of cylinder's surfaces. Since the cylinder radius is electrically small ($k_0 r \ll 1$), the magnetic currents can be assumed to be uniformly distributed over the cylinder perimeter, and modeled by line currents along the cylinder axes, namely, $M_n(l) \cong M_n$. In this way, the approximate boundary condition for zero total magnetic field at the centers of the cylinders $H_{\rm back}(x_m, y_m) + H_{\rm scat}(x_m, y_m) = 0$ for $m = 1, \ldots, N$ can be enforced to formulate the following $N \times N$ linear system of equations with respect to the unknown magnetic currents M_n:

$$\sum_{n=1}^{N} M_n [I_{mn} + 2\pi r G_{\rm smooth}(x_m, y_m, x_n, y_n)] = \frac{\eta_0}{jk_0} H_{\rm back}(x_m, y_m). \tag{16}$$

The quantity I_{mn} is the following approximately evaluated integral:

$$I_{mn} = \int_{(C_n)} G_{\text{singular}}(x_m, y_m, \chi(l), \psi(l))dl = -\frac{j\pi r}{2} \begin{cases} H_0^{(2)}(k_0 r), & m = n \\ H_0^{(2)}(k_0 d_{mn}), & m \neq n \end{cases} \quad (17)$$

where $d_{mn} = \sqrt{(x_m - x_n)^2 + (y_m - y_n)^2}$ is the distance between the centers of the nth and the mth particles.

In this way, the induced magnetic currents can be found and the scattered field in the far region (φ-dependent profile) takes the form

$$h_{\text{scat}}(\varphi) \sim -\frac{j2\pi k_0 r}{\eta_0} \sum_{n=1}^{N} M_n [e^{jk_0\rho_n \cos(\varphi-\varphi_n)} - \pi k_0 \cos\varphi S_{\text{gre}}(k_0 \sin\varphi) e^{-jk_0\rho_n \cos(\varphi+\varphi_n)}], \quad x \to -\infty \quad (18)$$

where $\rho_n = \sqrt{x_n^2 + y_n^2}$ and $\varphi_n = \arctan(x_n, y_n)$ are the polar coordinates of the cylindrical radiation vessels. Thus, we have obtained the analytical solution for the far field of the CML slab in the presence of numerous radiation vessels. In the following, we are going to use both approaches (circuit analysis and electromagnetic analysis) in order to study, interpret, and quantify the radiation enhancement achieved when the pins are located in the vicinity of the vacuum-CML interface.

V. NUMERICAL RESULTS

In the following examples, we use a large number of vessels which are positioned neither very close to each other, to avoid building effective PMC walls which will block the incident illumination, nor too far since we want a strong background field at their positions. In particular, we locate $N = 80$ random points (x_n, y_n) for $n = 1, \ldots, N$ belonging to a narrow vertical strip $\{-\lambda_0/20 < x < \lambda_0/20, -10\lambda_0 < y < 10\lambda_0\}$. The distance between every couple of centers of the cylinders d_{mn} is kept larger than $\lambda_0/5$, so that the lattice is inhomogeneous at the wavelength scale and there is strong diffuse scattering into the far zone [26]. As referred above, we confine ourselves to uniaxial media (under TM illumination) with

$$\varepsilon_t = \mu_t = a - jb, \quad \varepsilon_n = \frac{1}{\varepsilon_t} - j\delta = \frac{1}{a - jb} - j\delta, \quad (19)$$

and we are mainly interested in the CML cases with $a < 0$. Obviously, the presented results are dependent on the random distribution of the radiation vessels; however, our studies of a number of particular realizations of the pins distribution show that the obtained conclusions are valid regardless of the spatial distribution of the PMC pins in the vicinity of the CML slab.

A. Radiation enhancement

A metric of how strong is the effect of the radiation vessels on the radiated far-field strength should be definitely related with the energy of the azimuthal field profiles: $\{h_{\text{inc}}(\varphi), h_{\text{sec}}(\varphi), h_{\text{scat}}(\varphi)\}$. In particular, we can define the radiation enhancement ratio R as the ratio of the far-zone power radiated in the presence of the near-field scatterers over the corresponding quantity in the absence of them:

$$R = \frac{\int_{\pi/2}^{3\pi/2} |h(\varphi)|^2 d\varphi}{\int_{\pi/2}^{3\pi/2} |h_{\text{inc}}(\varphi) + h_{\text{sec}}(\varphi)|^2 d\varphi} \equiv \frac{\int_{\pi/2}^{3\pi/2} |h_{\text{inc}}(\varphi) + h_{\text{sec}}(\varphi) + h_{\text{scat}}(\varphi)|^2 d\varphi}{\int_{\pi/2}^{3\pi/2} |h_{\text{inc}}(\varphi) + h_{\text{sec}}(\varphi)|^2 d\varphi}. \quad (20)$$

Here, we evaluate and analyze the radiation enhancement factor R when certain parameters of the considered configuration vary. We are seeking for combinations of the structure, the material parameters, and the excitation which lead to $R \gg 1$, namely, a substantial improvement of the radiated power when one puts a random cluster of cylinders in the near region of the resonant surface.

In Fig. 5(a), we show the ratio R as a function of the real part a of the relative transversal permittivities/permeabilities ($a = \text{Re}[\varepsilon_t] = \text{Re}[\mu_t]$) for various perturbation parameters δ. One directly observes a huge change in the magnitude of R taking place when the material parameters transit from the double-negative (CML) slabs ($a < 0$) to double-positive, conventional PML slabs ($a > 0$). This feature is explained by the resonant nature of the CML with $a < 0$. That is why we are focusing on the case of CML ($a < 0$) rather than the conventional uniaxial PML ($a > 0$). With the purple dots, we show (in the DNG cases $a < 0$) the points on each curve for which the normal permittivity becomes lossless (it is lossy on the left side of the dots and active on the right side). In other words, the dots indicate the equality $\delta = \frac{b}{a^2+b^2} \Rightarrow a = -\sqrt{\frac{b}{\delta} - b^2}$, which is valid (within the considered ranges of a) only for the three of the four curves of Fig. 5(a) [and for none of Fig. 5(b)]. It is clear that when one moves along that "ultimate passivity boundary" (where none of the permittivity/permeability components are active) defined by the aforementioned successive purple dots, takes a decreasing R both for increasing δ and for increasing $a < 0$ (when $|a < 0|$ becomes smaller). We can also conclude that even when the medium is lossy for any direction of the fields, the radiation enhancement is significant.

Most importantly, these results prove that the radiation enhancement due to strong coupling of resonant surface modes to the far-field modes is orders of magnitude higher than possible reduction of radiation of propagating modes into the far zone. Recall that in the absence of the scatterers and $\delta \to 0$, the CML slab is perfectly matched to free space. For small values of b, all propagating modes are fully reflected, and we clearly see that adding pins makes the reflected fields more than two orders of magnitude stronger than reflected from a conventional perfect reflector. Furthermore, R is larger when δ is closer to zero which is anticipated by the limiting expression of (3) in the DNG case. The best results are recorded when a is negative but close to zero (much larger than -1, namely, for $-1 \ll a < 0$) where the radiation enhancement is giant and practically independent from δ. In Fig. 5(b), we represent R as a function of a for several loss parameters b. Again, we note that the cluster works only in the CML case, where it does a very good job ($R > 50$ on average). Finally, a smaller imaginary part b (with fixed $\delta > 0$) favors the increase in the radiated power achieved with the cylindrical vessels.

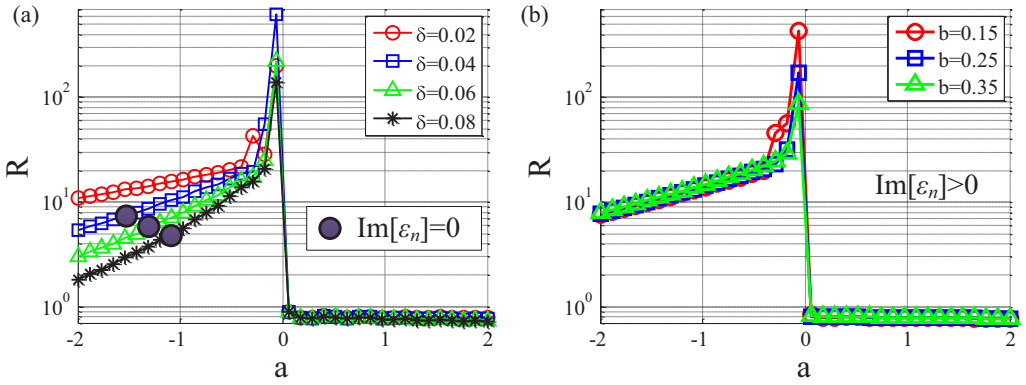

FIG. 5. The radiation enhancement ratio R as a function of the real part of the transversal components $a = \mathrm{Re}[\varepsilon_t] = \mathrm{Re}[\mu_t]$ for (a) several perturbation parameters $\delta = \mathrm{Im}[1/\varepsilon_t - \varepsilon_n]$ of the normal component of the material parameters (with $b = 0.1$) and (b) several values of the imaginary part $b = -\mathrm{Im}[\varepsilon_t] = -\mathrm{Im}[\mu_t]$ (with $\delta = 0.03$). Plot parameters: $r = \lambda_0/200$, $N = 80$, $g = \lambda_0/20$, $L = 3\lambda_0$, $\theta = 90^\circ$.

The singular behavior of the radiated power in the limit $a \to 0^-$ can be explained by considering the quality factor of the resonating surface modes. To do that, we calculate the equivalent inductance L_{CML} and resistance R_{CML} considering the wave impedance Z of the CML medium (2); similarly, one can find expressions for the capacitive effect of free space C_{VAC} by evaluating Z_0. If one assumes that $\delta > 0$ (to ensure overall passivity), evanescent modes $|k_t| > k_0$ (for which the interesting phenomena happen) and $a < 0$ (to have resonance), the quality factor of the equivalent RLC series circuit takes the form

$$Q = \frac{1}{R_{\mathrm{CML}}}\sqrt{\frac{L_{\mathrm{CML}}}{C_{\mathrm{VAC}}}} \Rightarrow$$

$$Q \cong \frac{\sqrt{2\left(k_t^2 - k_0^2\right)}}{k_t^2}\,\frac{\sqrt{2\left(k_t^2 - k_0^2\right) + b\delta k_t^2}}{(-a)\delta},\quad \delta \to 0^+. \quad (21)$$

It is easy to see that the loss parameter R_{CML} is proportional to $(-a)\delta$ in this case. Thus, for a fixed level of losses in the CML slab (measured by δ), the quality factor behaves as $1/a$ for $a \to 0^-$. Figure 6 shows the values of the quality factor on the plane

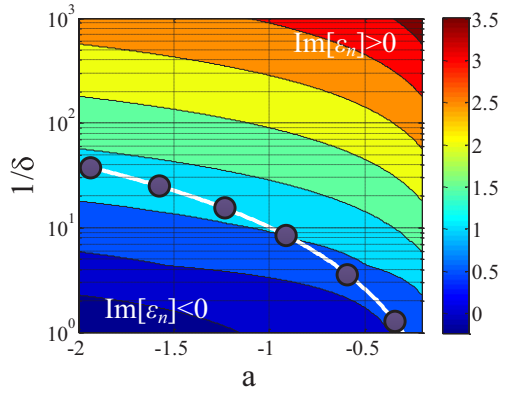

FIG. 6. The decimal logarithm of the quality factor of the equivalent circuit $\log Q$ with respect to the real part of the transversal components $a = \mathrm{Re}[\varepsilon_t] = \mathrm{Re}[\mu_t]$ and the inverse perturbation parameter $1/\delta = 1/\mathrm{Im}[1/\varepsilon_t - \varepsilon_n]$. Plot parameters: $k_t = 1.5k_0$, $b = 0.1$.

$(a, 1/\delta)$ in the region $-2 < a < 0.2$, $1 < 1/\delta < 100$. It is clear that Q obtains huge magnitudes when $|a|, \delta$ are very small for the CML scenario, namely, under the assumption of $a < 0$. The ultimate passivity boundary, along which we have a nonactive ε_n ($\mathrm{Im}[\varepsilon_n] = 0$), is indicated by a white line with purple dots. It divides the map $(a, 1/\delta)$ into two regions: one upper right which corresponds to active normal permittivity ($\mathrm{Im}[\varepsilon_n] > 0$) and one lower left which concerns a passive normal permittivity ($\mathrm{Im}[\varepsilon_n] < 0$).

In Fig. 7(a), we depict the variations of the radiation enhancement R with respect to the perturbation parameter $\delta = \mathrm{Im}[\frac{1}{\varepsilon_t} - \varepsilon_n] = \mathrm{Im}[\frac{1}{\mu_t} - \varepsilon_n]$ for several values of the real parts a of the transversal constituent components. When $\delta > 0$, namely, when the structure is overall passive, the effect of the radiation vessels becomes weaker and weaker for increasing δ, which is also obvious from Fig. 5(a). Note, however, that when the real part of the transversal permittivity approaches zero from negative values, radiated power enhancement remains substantial even for rather large positive δ, that is, for rather high overall losses in the system. On the other hand, when $\delta < 0$, the structure is overall active and the whole slab acts as an additional power source; that is why the variations are sharper and more parameter dependent. In particular, R possesses substantially oscillating and, on the average, much higher values when $\delta < 0$; in addition, the fluctuations are weaker and the output more stable when a is negative but close to zero. It should be pointed out that these "spikes" in the response of the active structures reminds of electrical thickness resonances combined with a proper excitation. As it will be illustrated later in the analysis, such behavior is not attributed mainly to the presence of a random grid of pins but to the fact that the grounded slab is active and infinite in size. Again, one can observe the behavior of the system along the "ultimate passivity limit" (purple dots) which indicate once again that the functions $R = R(\delta > 0)$ and $R = R(a < 0)$ are decreasing.

In Fig. 7(b), the change of $R = R(\delta)$ is shown for various $b = \mathrm{Im}[\varepsilon_t] = \mathrm{Im}[\mu_t]$. The radiation enhancement is almost independent from the imaginary part b in the passive scenario, while, similarly to Fig. 7(a), shaky response is observed when $\delta < 0$. It appears that when the system is overall active, one can find specific narrow intervals of δ where extremely high

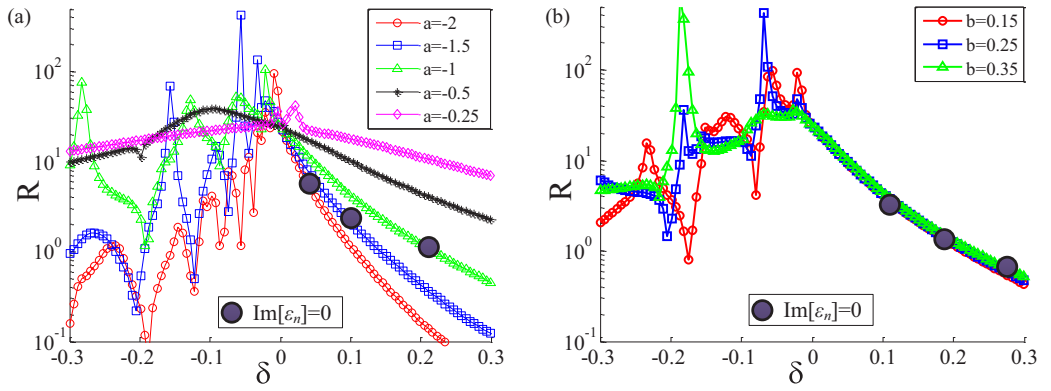

FIG. 7. The radiation enhancement ratio R as function of the perturbation parameter $\delta = \mathrm{Im}[1/\varepsilon_t - \varepsilon_n]$ for (a) various real part of transversal components $a = \mathrm{Re}[\varepsilon_t] = \mathrm{Re}[\mu_t]$ (with $b = 0.2$) and (b) various imaginary parts $b = -\mathrm{Im}[\varepsilon_t] = -\mathrm{Im}[\mu_t]$ (with $a = -1$). Plot parameters: $r = \lambda_0/200$, $N = 80$, $g = \lambda_0/20$, $L = 3\lambda_0$, $\theta = 90^\circ$.

radiation is achieved regardless of the inherent losses b along the transversal directions.

As far as the rapid oscillations of the device response for $\delta < 0$ are concerned, we show in Fig. 8(a) the reflection coefficient when the radiation vessels are absent and the structure is illuminated by an obliquely incident propagating plane wave. In Fig. 8(a), we represent the decimal logarithm of the reflection coefficient with respect to the perturbation parameter of the imaginary part δ and the incidence angle. Apparently, the reflection coefficient can be larger than unity for the active case ($\delta < 0$); furthermore, sharp maxima are recorded for the same half-plane close to the grazing angle. In other words, similar "spikes" as those appearing in Fig. 7 constitute a characteristic of the active structure even though no evanescent modes are considered (real incidence angles) and no radiation vessels are used. They are just resonances of an infinite active slab which pumps energy to the system occurring at specific excitation directions. To better understand how these oscillations depend on the real part of the transversal permittivity/permeability of the CML, we show [Fig. 8(b)] the average magnitude of the aforementioned reflection coefficient (with respect to the real incidence angle) as a function of δ for several a. It is clear that the number of peaks increases for more negative a and most of them are exhibited for $\delta \to 0^-$; such a conclusion is compatible with the variations in Fig. 7(a). Finally, the curve spikes in Fig. 8(b) do not appear at the same δ as those in Fig. 7(a) since they correspond to different systems (excitation and structure); however, the inherent tendency of the active slab ($\delta < 0$) towards abruptly changing response is demonstrated in both cases.

A more systematic approach which proves the necessity of an overall active slab ($\delta < 0$) in order to have sharp maxima comes from the corresponding transmission-line model of the grounded CML slab. The reflection coefficient of a vessel-free structure [which is represented in Fig. 8(a)] is written in terms of the TM wave impedances (2) as follows: $RC = \frac{Z_0 - Z\tanh[\kappa(k_t)L]}{Z_0 + Z\tanh[\kappa(k_t)L]}$. The quantity RC has large (or infinite) magnitude, which imply sharp variations, when its denominator takes small (or zero) values. It is more feasible when the argument of hyperbolic tangent is an imaginary number; it is then replaced by a trigonometric tangent whose range is infinite and thus the equality $Z_0 + Z\tanh[\kappa(k_t)L] = 0$ becomes easier to get (even approximately) satisfied. Such a condition can only be fulfilled when quantity under the square root of $\kappa(k_t)$ is negative and thus purely real, namely, when $\mathrm{Im}[\kappa^2(k_t)] = 0 \Rightarrow k_t^2 = 2bk_0^2(\frac{1}{2b-(a^2+b^2)\delta} - \delta)$. For this

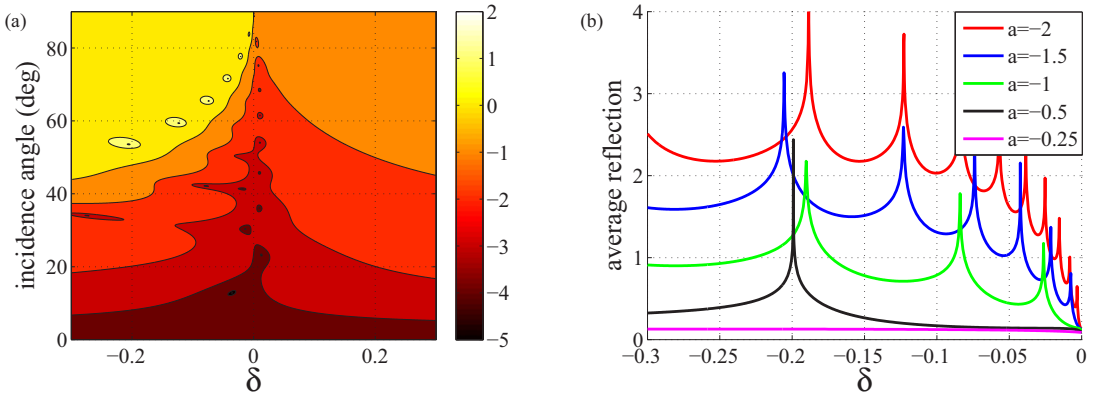

FIG. 8. (a) The decimal logarithm of the magnitude of the reflection coefficient of the vessel-free structure as function of the perturbation of the imaginary part δ and the incidence angle (with $a = -1.5$). (b) The average magnitude of the reflection coefficient over all the real incidence angles as function of the perturbation δ for various real parts of transversal components a. Plot parameters: $b = 0.2$, $L = 3\lambda_0$.

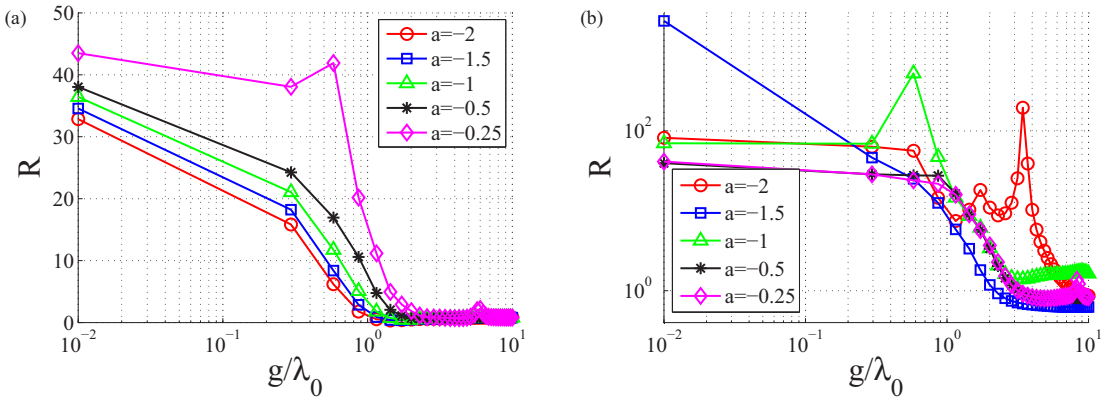

FIG. 9. The radiation enhancement ratio R for various values of the real part of transversal components $a = \mathrm{Re}[\varepsilon_t] = \mathrm{Re}[\mu_t]$ as a function of the electrical distance of the source from the interface g/λ_0 ($L = 3\lambda_0$). (a) Overall passive CML with $\delta = 0.02$. (b) Overall active CML with $\delta = -0.02$. Plot parameters: $b = 0.2$, $r = \lambda_0/200$, $N = 80$, $\theta = 90^\circ$.

direction of excitation, the propagation constant in the CML slab is real and takes the form $\kappa \cong k_0 \frac{a^2+b^2}{\sqrt{2}b}\sqrt{\delta}$ for small $\delta \to 0$. It is now clear that the only way for the quantity $\tanh[\kappa(k_t)L]$ to have the sharp variations of the trigonometric tangent is to use an overall active structure with $\delta < 0$ (given that $b > 0$).

In Fig. 9, we identify the influence of the location of the primary source in representative passive and active scenarios ($\delta = \pm 0.02$). In Fig. 9(a), we can see that the radiation falls rapidly as the primary source gets distant from the air-CML slab interface because the evanescent part of the exciting field gets weaker. However, especially in the active case shown in Fig. 9(b), radiation enhancement remains significant even when the distance to the source is much larger than the wavelength. As indicated above, in the active case the enhancement factor R takes, on the average, higher values and exhibits a less monotonic behavior as a function of the geometrical and material parameters of the configurations.

B. Radiation patterns

Apart from the macroscopic insight offered by the radiation-enhancement metric R, one can understand many features by observing the azimuthal variations of the far-field patterns for the introduced radiation-enhancing mirrors. The represented quantities are normalized by $|h_{\mathrm{inc}}(0)| = k_0\omega q/4$. The incident field in the far region $h_{\mathrm{inc}}(\varphi)$ is evaluated by (7), the background field $h_{\mathrm{inc}}(\varphi) + h_{\mathrm{sec}}(\varphi)$ is given by (8), and the total field in the presence of the cylinders $h_{\mathrm{inc}}(\varphi) + h_{\mathrm{sec}}(\varphi) + h_{\mathrm{scat}}(\varphi)$ is computed using (18).

In Fig. 10, we illustrate two characteristic cases: one passive [Fig. 10(a)] and one active [Fig. 10(b)]. The far-field patterns are represented in the case that the grounded CML slab is nearly fully reflecting propagating waves (we select the dissipation parameter $b = 0$ and the CML loss factor δ is small). The three curves compare the far-field pattern of the primary source into free space (green), the pattern for the CML slab without perturbing pins (blue), and the CML slab with radiation enhancing vessels (red). The green curve is simply the pattern of a dipole line source, with the maximum in the broadside direction [in both Figs. 10(a) and 10(b)]. CML slab without pins basically acts as a reflector for the propagating part of the incident spectrum and its response gets substantially enhanced along the grazing-angle directions ($\varphi \cong 90^\circ, 270^\circ$) for the active scenario. We can see that for the passive mirror the maximum enhancement of the field strength equals 2 (fourfold in terms of power), which takes place for directions along which

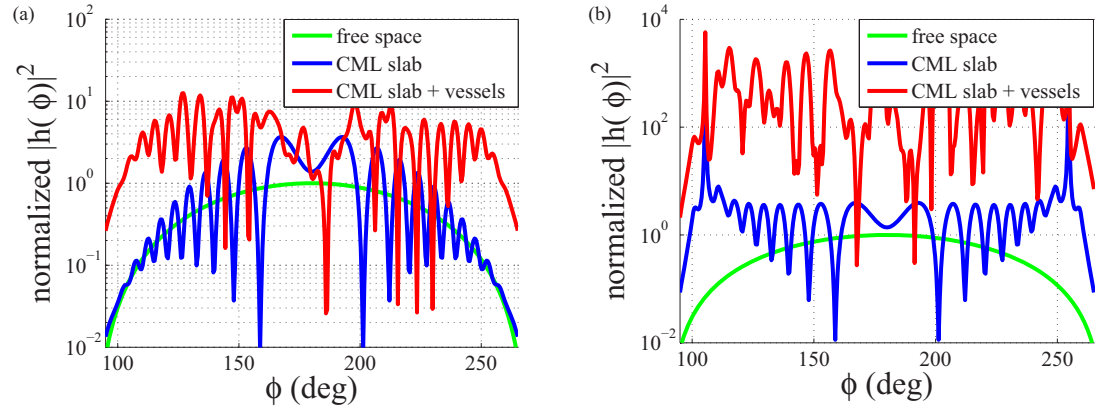

FIG. 10. The azimuthal profiles $|h(\varphi)|^2$ (normalized by $|h_{\mathrm{inc}}(0)|^2 = k_0^2\omega^2 q^2/16$) of the incident field, the background field and the total field as functions of angle φ for: (a) a passive scenario ($\delta = +0.01$) and (b) an active scenario ($\delta = -0.01$). Plot parameters: $a = -2$, $b = 0$, $L = 3\lambda_0$, $g\lambda_0/10$, $r = \lambda_0/100$, $N = 80$, $\theta = 90^\circ$.

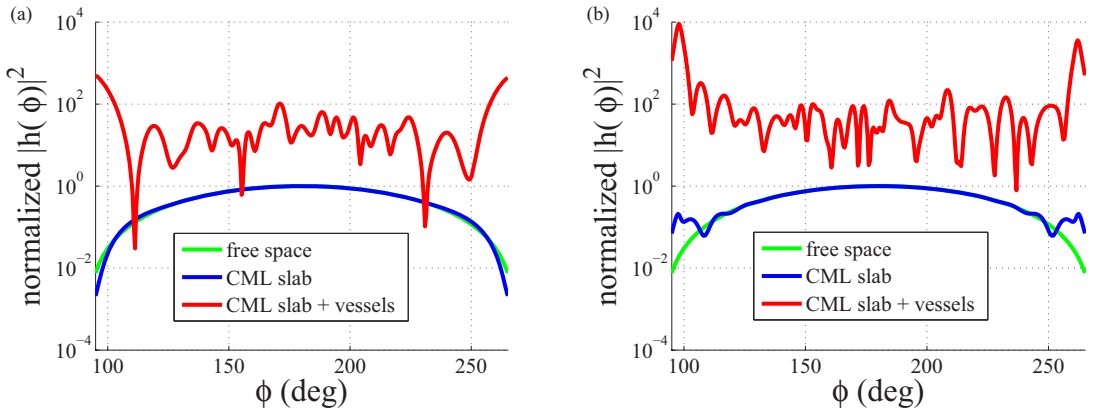

FIG. 11. The azimuthal profiles $|h(\varphi)|^2$ [normalized by $|h_{\rm inc}(0)|^2 = k_0^2\omega^2 q^2/16$] of the incident field, the background field, and the total field for (a) $a = -0.25$, $\delta = 0.02$, $L = 2.557\lambda_0$, $g = \lambda_0/20$ ($R \cong 84$) and (b) $a = -1$, $\delta = -0.02$, $L = 3\lambda_0$, $g = 0.0665\lambda_0$ ($R \cong 525$). Plot parameters: $b = 0.2$, $r = \lambda_0/200$, $N = 80$, $\theta = 90^\circ$.

the reflected field sums up in phase with the field of the primary source. This value is the maximal possible value of the reflected field from any ideally reflecting planar mirror (with arbitrary reflection phase). We clearly see that the radiation vessels provide an additional radiation channel via the evanescent part of the spectrum, and the radiated power is strongly enhanced, well above the fundamental limit for any lossless mirror.

In Fig. 11, we represent the results also for a passive [Fig. 11(a)] and an active [Fig. 11(b)] case which correspond to high radiation enhancement R. Losses in the CML are present ($b = 0.2$), so that the reflections of the propagating part of incident waves are weak. That is why we see that the blue and green curves nearly coincide for the passive CML. The chosen value of $\delta = 0.02$ leads to an enhancement in radiation by a factor of $R \cong 84$. In this case, it is apparent that the far-field response of the CML slab without the radiation enhancing cluster is almost identical to the incident field, which is anticipated from (8). However, when one puts the randomly distributed vessels in the near field, the output power of the antenna gets significantly amplified (and the pattern becomes asymmetric with respect to $\varphi = 180^\circ$). In Fig. 11(b), corresponding to an active CML, we use $\delta = -0.02$ and the enhancement is huge in all directions (the overall radiated power enhancement factor $R \cong 525$).

All the proposed structures used in the aforementioned cases incorporate as the main component the CML medium, a material whose effective properties are described above. For this reason, the issue of actually realizing DNG structures with controllable values of the longitudinal parameters may be raised. To emulate the negative transversal permittivities and permeabilities, one of the most promising configurations is the so-called fishnet structure [27,28]; a multilayered structure of perforated thin metal sheets. As far as the longitudinal direction is concerned, one can insert into the formed holes rods of negative permittivity materials or wire media to achieve the desired response. A more detailed description on how materials with CML properties may be constructed is contained in [13].

VI. CONCLUSIONS

It is well known that infinite homogeneous planar surfaces can fully reflect electromagnetic waves in the limit of negligible losses. In this case, the amplitude of waves radiated by a source near the mirror can be doubled as compared with the incident waves. This surface is thought to be "ideally shiny." On the other hand, the reflection coefficient from planar surfaces can be, in principle, made zero for all incident propagating waves (any polarization and any incident angle). In this case, all power of incident propagating plane waves is absorbed and the surface is "ideally black," absorbing maximum power and, reciprocally, emitting maximal heat power according to the Plank law. In both these scenarios, evanescent waves do not participate in power exchange between far-zone external sources and the material body.

In this paper, we have shown that perturbing the boundary of an infinite planar surface which maintains resonant surface modes, can in principle realize a planar reflector which reflects more power than any ideally reflecting planar surface. Due to perturbations, surface modes couple to propagating plane waves and create additional channels for power exchange via evanescent fields. Such perturbed resonant surface extracts extra power from near sources and sends that into space. The amplitude of the reflected field can be orders of magnitude larger than the maximal value of 2 for any usual lossless mirror. Making the perturbation lossy, it can become possible to overcome the black-body limit even for planar surfaces. In this scenario, the black body absorbs nearly all propagating waves, while the perturbations provide coupling between the resonant surface modes and an additional energy sink via evanescent modes.

The perturbations are random at the wavelength scale and nonresonant. In this configuration, the surface-averaged currents induced in the perturbation objects (which could partially reflect propagating waves and compromise their absorption in the CML body) are small because they couple to nonresonant propagating modes of the absorbing or reflecting body. On the other hand, current components which vary fast on the wavelength scale can be huge because they couple to highly resonant CML body. These spatially inhomogeneous resonant currents on the perturbations provide additional channels for power exchange between the body and free-space wave modes, allowing stronger reflections than from an ideal reflector or more absorption than in the ideal black body.

Analyzing the far-zone radiation patterns, we see that there is an analogy between the revealed phenomena and superdirectivity of antennas [29]. Superdirective radiators can create a narrow beam with the directivity higher than that of the same configuration which is uniformly excited [30]. However, in the configuration which we have introduced here, it appears that the planar reflector sends superdirective beams nearly everywhere (pattern oscillations are determined by random positions of radiation vessels). There is also a connection of the revealed phenomena to the concept of perfect lens as a slab of a lossless double-negative material [31]. The perfect lens operation also exploits resonance of surface modes at an interface between free space and a double-negative material. In the perfect lens concept, high-amplitude reactive fields at the entry interface are focused behind the lens thanks to interactions between resonant modes of the two parallel surfaces of the lens. In papers [12,13], it was shown how the reactive energy of the resonant surface modes can be fully absorbed. Here, we have shown that this energy can be launched into space, creating super-reflectors and far-field superemitters.

This study is relevant also to the technologies of wireless power transfer. In order to ensure the fastest wireless energy transfer from a source to the user, one needs to maximize the channel capacity for power transport. In communications technologies, the concept of MIMO (multiple input, multiple output) exploits the idea of sending signals via many different rays which may reach the receiver. However, if we are concerned with the task of *energy* transfer, still only one mode is conventionally exploited, even if multiple antennas are used to send power to the receiver. In the near-field scenario, this is the magnetic dipole mode of receiving coil antennas. In the far-field scenario, this is the propagating plane wave (transverse electromagnetic, TEM) mode. Here, we have shown how a multichannel wireless power transfer can be in principle realized.

Although in this paper we have considered a particular realization of surface perturbations in the form of a random array of thin cylinders, the concept is general and the surface can be perturbed in many various ways, for instance, simply making the surface rough at the appropriate wavelength scale. Likewise, the surface does not have to be planar or infinite: properly perturbing the surface of a finite-size conjugately matched body we can dramatically enhance its coupling to electromagnetic fields in space. Discussed superemission and superabsorption phenomena can potentially enable new approaches to optimizing wireless transfer of energy or information and in radiative heat transfer management.

[1] C. M. Watts, X. Liu, and W. J. Padilla, Metamaterial electromagnetic wave absorbers, Adv. Mater. **24**, OP98 (2012).

[2] Y. Radi, C. R. Simovski, and S. A. Tretyakov, Thin perfect absorbers for electromagnetic waves: Theory, design, and realizations, Phys. Rev. Appl. **3**, 037001 (2015).

[3] E. E. Narimanov and A. V. Kildishev, Optical black hole: Broadband omnidirectional light absorber, Appl. Phys. Lett. **95**, 041106 (2009).

[4] Q. Cheng, T. J. Cui, W. X. Jiang, and B. G. Cai, An omnidirectional electromagnetic absorber made of metamaterials, New J. Phys. **12**, 063006 (2010).

[5] S.-A. Biehs, M. Tschikin, and P. Ben-Abdallah, Hyperbolic Metamaterials as An Analog of a Blackbody in the Near Field, Phys. Rev. Lett. **109**, 104301 (2012).

[6] C. Simovski, S. Maslovski, I. Nefedov, and S. Tretyakov, Optimization of radiative heat transfer in hyperbolic metamaterials for thermophotovoltaic applications, Opt. Express **21**, 14988 (2013).

[7] N. Mohammadi Estakhri and A. Alù, Minimum-scattering superabsorbers, Phys. Rev. B **89**, 121416(R) (2014).

[8] D.-H. Kwon and D. M. Pozar, Optimal characteristics of an arbitrary receive antenna, IEEE Trans. Antennas Propag. **57**, 3720 (2009).

[9] C. F. Bohren and D. R. Huffman, *Absorption and Scattering of Light by Small Particles* (Wiley, Weinheim, 2007), p. 129.

[10] G. Kirchhoff, On the relation between the radiating and absorbing powers of different bodies for light and heat, Philos. Mag. **4**, 1 (1860).

[11] M. Planck, *The Theory of Heat Radiation*, 2nd. ed. translated by M. Masius (P. Blakiston's Son, Philadelphia, 1914).

[12] S. I. Maslovski, C. R. Simovski, and S. A. Tretyakov, Overcoming black body radiation limit in free space: Metamaterial superemitter, New J. Phys. **18**, 013034 (2016).

[13] C. A. Valagiannopoulos, J. Vehmas, C. R. Simovski, S. A. Tretyakov, and S. Maslovski, Electromagnetic energy sink, Phys. Rev. B **92**, 245402 (2015).

[14] Y. I. Bobrovnitskii, Impedance theory of sound absorption: The best absorber and the black body, Acoust. Phys. **52**, 638 (2006).

[15] L. N. Zakhariev and A. A. Lemanski, *Scattering of Waves by "Black" Bodies* (Sovetskoje Radio 34, Moscow, 1972) (in Russian).

[16] S. D. Gedney, An anisotropic perfectly matched layer-absorbing medium for the truncation of FDTD lattices, IEEE Trans. Antennas Propag. **44**, 1630 (1996).

[17] R. W. Ziolkowski, The design of Maxwellian absorbers for numerical boundary conditions and for practical applications using artificial engineered materials, IEEE Trans. Antennas Propag. **45**, 656 (1997).

[18] F. L. Teixeira and W. C. Chew, General closed-form PML constitutive tensors to match arbitrary bianisotropic and dispersive linear media, IEEE Microwave Guided Wave Lett. **8**, 223 (1998).

[19] S. A. Tretyakov and T. G. Kharina, The perfectly matched layer as a synthetic material with active inclusions, Electromagnetics **20**, 155 (2000).

[20] N. Tedeschi, F. Frezza, and A. Sihvola, On the perfectly matched layer and the DB boundary condition, J. Opt. Soc. Am. A **30**, 1941 (2013).

[21] V. G. Veselago, The electrodynamics of substances with simultaneously negative values of ϵ and μ, Usp. Fiz. Nauk **92**, 517 (1967) [Sov. Phys.–Usp. **10**, 509 (1968)].

[22] C. A. Valagiannopoulos, M. S. Mirmoosa, I. S. Nefedov, S. A. Tretyakov and C. R. Simovski, Hyperbolic-metamaterial

antennas for broadband enhancement of dipole emission to free space, J. Appl. Phys. **116**, 163106 (2014).

[23] L. B. Felsen and N. Marcuvitz, *Radiation and Scattering of Waves*, IEEE Series on Electromagnetic Wave Theory (Wiley, Hoboken, NJ, 1972).

[24] C. A. Valagiannopoulos, On examining the influence of a thin dielectric strip posed across the diameter of a penetrable radiating cylinder, Prog. Electromagn. Res. C **3**, 203 (2008).

[25] C. A. Valagiannopoulos, Study of an electrically anisotropic cylinder excited magnetically by a straight strip line, Prog. Electromagn. Res. C **73**, 297 (2007).

[26] S. A. Tretyakov, *Analytical Modeling in Applied Electromagnetics* (Artech House, London, 2003).

[27] J. Valentine, S. Zhang, T. Zentgraf, E. Ulin-Avila, D. A. Genov, G. Bartal, and X. Zhang, Three-dimensional optical metamaterial with a negative refractive index, Nature (London) **455**, 376 (2008).

[28] M. Kafesaki, I. Tsiapa, N. Katsarakis, Th. Koschny, C. M. Soukoulis, and E. N. Economou, Left-handed metamaterials: The fishnet structure and its variations, Phys. Rev. B **75**, 235114 (2007).

[29] S. A. Schelkunoff, A mathematical theory of linear arrays, Bell Syst. Tech. J. **22**, 80 (1943).

[30] R. C. Hansen, Fundamental limitations in antennas, Proc. IEEE **69**, 170 (1981).

[31] J. B. Pendry, Negative Refraction Makes a Perfect Lens, Phys. Rev. Lett. **85**, 3966 (2000).